Dual roles of *f* electrons in mixing Al 3*p* character into *d*-orbital conduction bands for lanthanide and actinide dialuminides

Alison B. Altman,[1,2] C. D. Pemmaraju,[1] Selim Alayoglu,[1] John Arnold,[1,2] Eric D. Bauer,[3] Corwin H. Booth,[1] Zachary Fisk,[4] Joseph I. Pacold,[1] David Prendergast,[1] David K. Shuh,[1] Tolek Tyliszczak,[1] Jian Wang,[5] and Stefan G. Minasian[1,*]
[1]*Lawrence Berkeley National Laboratory, Berkeley, Berkeley, California 94720, USA*
[2]*University of California, Berkeley, Berkeley, California 94720, USA*
[3]*Los Alamos National Laboratory, Los Alamos, New Mexico 87545, USA*
[4]*University of California, Irvine, Irvine, California 92697, USA*
[5]*Canadian Light Source, Saskatoon, Saskatchewan, Canada, S7N 2V3*

(Received 4 August 2017; revised manuscript received 18 October 2017; published 10 January 2018)

Correlated electron phenomena in lanthanide and actinide materials are driven by a complex interplay between the f and d orbitals. In this study, aluminum K-edge x-ray absorption spectroscopy and density functional theory calculations are used to evaluate the electronic structure of the dialuminides, MAl$_2$ (M = Ce, Sm, Eu, Yb, Lu, U, and Pu). The results show how the energy and occupancy of the 4f or 5f orbitals impacts mixing of Al 3p character into the 5d or 6d conduction bands, which has implications for understanding the magnetic and structural properties of correlated electron systems.

DOI: 10.1103/PhysRevB.97.045110

I. INTRODUCTION

Considerable progress has been made towards unraveling the complex electronic properties of correlated electron systems based on actinide elements. Many of these studies challenge the traditional viewpoint that actinide-based electrons are housed in corelike 5f orbitals and that magnetic properties arise solely from the spin and orbital angular momenta of the unpaired electrons [1–8]. For more than 60 years, lanthanide and actinide dialuminides (LnAl$_2$ and AnAl$_2$) have been employed as prototypical correlated electron systems because they all have the same cubic Cu_2Mg structure. Although the LnAl$_2$ are generally ferromagnets (FMs) [9], there are important exceptions. CeAl$_2$ is an antiferromagnet (AFM) [10] and shows quantum critical behavior resulting from 4f-orbital hybridization with the 5d conduction band [11,12]. EuAl$_2$ and YbAl$_2$ are more overtly multiconfigurational [13–15]; for example, YbAl$_2$ is best described by an interaction of both Yb^{3+} (4f^{13}) and Yb^{2+} (4f^{14}) configurations [16–18]. Building on this simple intermediate valence scenario, optical conductivity [19,20] and magnetic susceptibility measurements [17,21,22] have revealed an itinerancy and localization duality in which coupling of the localized 4f electrons to the more delocalized 5d states can impact the mechanisms of electrical conduction and quenching of magnetic moments. These observations support a model in which close proximity of 4f bands to the Fermi energy perturbs the 5d conduction band, resulting in unusual Kondo and heavy fermion effects [23–26]. Of the known AnAl$_2$ analogs [27], UAl$_2$ is a spin-fluctuation compound with a temperature scale of 15 K [28], NpAl$_2$ is a FM below 56 K [29], and PuAl$_2$ has complicated low-temperature properties including an AFM transition at 3.5 K [30]. In fact, UAl$_2$, NpAl$_2$, and PuAl$_2$ are examples of the failure of the Hill criterion for describing magnetic ground states [31,32] since they have similar An–An distances (3.365–3.391 Å), yet very different magnetic ground states. The ability of 6d orbitals to mediate 5f electron behavior and magnetic properties is still difficult to probe experimentally, and theoretical treatments for extended solids require demanding approaches to include relativistic and many-body effects while also accounting for partial electron delocalization and multiconfigurational ground states [33].

Aluminum K-edge x-ray absorption spectroscopy (XAS) probes dipole-allowed transitions from core Al 1s orbitals to final states with Al 3p-orbital character and can be employed for LnAl$_2$ and AnAl$_2$ to provide electronic structure insights that would be difficult to obtain using other techniques. Al K-edge XAS uses x rays in the 1555–1570 eV range where edge features are easily resolved; core-hole lifetime broadening at the Al K edge is approximately 0.4 eV, versus 3.2 and 8.7 eV for typical cerium and uranium L_3-edge measurements [34]. Combined with an instrumental resolution approaching 0.2 eV, this energy resolution provides an opportunity to move beyond valence formulations and to form interpretations within a band structure model. However, because many synchrotron beamlines are not optimized in the energy regime that includes the Al K edge, measurements are often subject to reduced photon flux and require sample preparation methodologies that lead to significant self-absorption and saturation effects. To the best of our knowledge, Al K-edge XAS has not been used to characterize lanthanide or actinide electronic structure and is generally limited to, for example, studies of aluminum metal [35,36], oxides and minerals [37,38], zeolites [39–41], and a small number of synthetic materials [42–44].

This article describes the use of Al K-edge XAS as a direct experimental probe of itinerancy and localization in LnAl$_2$ and

*Corresponding author: sgminasian@lbl.gov

AnAl_2 compounds (*Ln* = Ce, Sm, Eu, Yb, Lu; *An* = U, Pu). Samples were analyzed using a scanning transmission x-ray microscope (STXM) to provide Al *K*-edge data from micron-sized particles with simultaneous minimization of x-ray self-absorption. STXM diminishes the need for supplementary windows or chambers normally used for radiological containment, thus overcoming challenges with photon attenuation that can preclude spectroscopic investigation of actinide samples using soft x rays. Spectroscopic signatures of orbital mixing are identified with the aid of hybrid DFT calculations, which shows transitions into new Al 3*p*- and *Ln* 5*d*- or *An* 6*d*-orbital bonding states at low energy in the conduction band. Intuitive models are presented to contextualize these results and account for the role of *d* orbitals in mediating behavior of the *f* electrons by allowing them to appear localized while simultaneously impacting magnetic moments and participating indirectly in the conduction band. Changes in dialuminide stability with variations in the energy and occupancy of the 4*f* and 5*f* orbitals are also discussed.

II. METHODS

A. Synthesis and characterization

Polycrystalline $CeAl_2$, $YbAl_2$, $LuAl_2$, UAl_2, and $PuAl_2$ materials were prepared by arc melting the elements in stoichiometric amounts on a water-cooled copper hearth under an argon atmosphere with a Zr getter. $PuAl_2$ was wrapped in Ta foil, sealed in a silica tube under vacuum, and annealed at 600 °C for 3 days. X-ray diffraction measurements confirmed single-phase material for $CeAl_2$, $YbAl_2$, $LuAl_2$, UAl_2, and $PuAl_2$. Samples of $EuAl_2$ and $SmAl_2$ were prepared by induction melting stoichiometric amounts of the elements in sealed Ta tubes. About 0.8 g of $EuAl_2$ and 0.5 g of $SmAl_2$ were heated up to 1400 °C and 1520 °C, respectively, over about 15 min, then quenched rapidly ($\sim 200-300\,^{\circ}$C/min) by turning off the induction melter. The temperature was measured using an optical pyrometer with an accuracy of +/−50 °C. X-ray diffraction measurements revealed about 70% $EuAl_2$ and 30% $EuAl_4$ present in the as-cast sample. The $EuAl_2$ as-cast sample was wrapped in Ta foil, sealed in a silica tube under vacuum, and annealed at 1000 °C for 6 days to improve phase purity. The as-cast $SmAl_2$ sample contained about 95% $SmAl_2$, along with 5% $SmAl_3$ and trace amounts of SmAl. No further heat treatment was performed on the $SmAl_2$ sample. Radiation damage can be significant at low temperatures for plutonium metal and intermetallics including $PuAl_2$, but previous research has shown that self-annealing at room temperature repairs many defects [45,46]. To evaluate the possible effects of radiation damage in this study, measurements were reproduced on the same sample over multiple beam runs spanning a range of approximately 10 years.

B. Al *K*-edge STXM-XAS measurements

STXM-XAS methodology was similar to that previously described [42,47]. Samples were prepared by grinding crystals of the analyte into a fine powder with a mortar and pestle and brushing the powder onto a Si_3N_4 membrane (100 nm, Silson) or carbon support films (3–4 nm carbon, 10 nm formvar, Electron Microscopy Sciences) with a fiber, which arranged a large number of micron-sized particles in a compact area suitable for Al *K*-edge XAS. Radioactive samples were sealed between two membranes using Hardman Double/Bubble 5-minute epoxy. Single energy images, elemental maps, Al *K*-edge and Sm and Eu $M_{5,4}$- edge spectra were acquired using STXM-XAS instruments at both the Molecular Environmental Science (MES) beamline 11.0.2 at the Advanced Light Source (ALS), which is operated in top-off mode (500 mA), and the spectromicroscopy beamline 10ID-1 at the Canadian Light Source (CLS), which is operated in decay mode (250–150 mA). At both instruments, data were collected under a ~0.5 atm helium atmosphere. The beamlines use photons from elliptically polarizing undulators that deliver photons in the 130–2700 eV range (CLS) [48] and in the 100–2000 eV range (ALS) [49–51] to an entrance slitless-variable-included angle plane-grating monochromator. Under normal conditions, variations in beamline energy calibration and performance between experimental periods would lead to significant differences in transition energies exceeding ±0.3 eV. For these experiments, a primary set of single scans was collected for each sample in rapid succession during the same run, and standard deviation in transition energies of ±0.2 eV was established. This primary set of scans was calibrated to the Al *K* edge of a 1000-Å aluminum filter sample (Luxel, inflection poin t = 1559.0 eV). Additional spectra obtained from multiple particles and experimental runs were shifted accordingly to match the primary set and then averaged to achieve the best possible data quality and signal-to-background ratio.

For all these measurements, the x-ray beam was focused with a zone plate onto the sample and the transmitted light was detected. The spot size and spectral resolution were determined from characteristics of the 40-nm zone plate at ALS and 35 nm at CLS. Images at a single energy were obtained by raster-scanning the sample and collecting transmitted monochromatic light as a function of sample position (Fig. S9). Spectra at particular regions of interest on the sample image were extracted from the "stack," which is a collection of images recorded at multiple, closely spaced photon energies across the absorption edge. Dwell times used to acquire an image at a single photon energy were 1 or 2 ms per pixel and spectra were obtained using horizontally polarized radiation. To quantify the absorbance signal, the measured transmitted intensity (I) was converted to optical density using the Beer-Lambert law: OD = $\ln(I/I_0) = \mu\rho d$, where I_0 is the incident photon flux intensity, d is the sample thickness, and μ and ρ are the mass absorption coefficients and density of the sample material, respectively. Incident beam intensity was measured through the particle-free region of the samples. Regions of particles with absorption of >1.5 OD were omitted. Because the density of $M Al_2$ intermetallics is high (4.9−8.3 g cm^{-3} for $CeAl_2$ and UAl_2, respectively), small sizes on the order of 0.25−1 μm^2 were typically required to ensure the spectra were in the linear regime of the Beer-Lambert law (see Fig. S9). Multiple spectra from different particles and beam runs were collected and then averaged to improve data quality and signal-to-background ratio. In the case of the $PuAl_2$ sample, spectra were collected over multiple years to ensure radiation damage was not distorting the observed spectra.

C. Data analysis

The Al K-edge data for $CeAl_2$, $EuAl_2$, UAl_2, and $PuAl_2$ were background subtracted and normalized using the MBACK algorithm in MATLAB [52]. For $SmAl_2$, $YbAl_2$, and $LuAl_2$, the Al K-edge spectra coincided with additional absorptions, including the Sm M_2 edge at 1547 eV, the Yb $M_{5,4}$ edges at 1519.8 and ~1576 eV, and the Lu M_5 edge at ~1600 eV. For these datasets, a line was fit to the preedge region below 1556 eV for $YbAl_2$ and $LuAl_2$, and 1536 eV for $SmAl_2$, and then subtracted from the experimental data to eliminate the background of the spectrum. The data were normalized by fitting a first-order polynomial to the postedge region of the spectrum, 1570−1588 eV for $LuAl_2$ and 1570−1700 for $SmAl_2$ and $YbAl_2$, and setting the edge jump at 1570 eV to an intensity of 1.0. In the case of $YbAl_2$, the data were normalized based on the $EuAl_2$ spectrum by scaling the data to match the intensity of the broad, intense feature near 1565 eV.

Fits for the preedge region of the Al K-edge data for the $M Al_2$ spectra were generated using the program IGOR 6.0 and a modified version of EDG_FIT [53]. The second derivatives of the spectra were used as guides for the number and position of preedge peaks, which were modeled using pseudo-Voigt line shapes consisting of an equal mixture of Gaussian and Lorentzian character in addition to a step function with a 1:1 ratio of arctangent and error function contributions that were used to model the rising edge. These analyses provided high-quality fits of the experimental data that were consistent between the systems as reflected by low-correlation coefficients, residual data that deviated slightly from zero, and symmetric residual peaks that matched well with the parent pseudo-Voigt functions. For each $M Al_2$ intermetallic, two pseudo-Voigt functions and a step function were used to model the high-energy peak and the postedge. For $EuAl_2$, $YbAl_2$, and $LuAl_2$, three features are well-resolved in the low-energy region below 1562 eV, and their energies and intensities have been determined from the three corresponding curve-fit functions. For $CeAl_2$, $SmAl_2$, UAl_2, and $PuAl_2$, the first and second derivatives of the data and the curve-fitting analysis also indicate that three pseudo-Voigt functions are necessary to describe the region below 1562 eV. For $CeAl_2$, UAl_2, and $PuAl_2$, fully unconstrained deconvolutions did not converge with step energy values that were consistent with the values generated by the fitting procedure for the other intermetallics. To obtain a consistent model, it was necessary to constrain the step-function energy in these spectra to an energy greater than or equal to 1562.5 eV. Spectral intensities and energies were determined from the position and area, respectively, of the corresponding curve-fit functions. Errors in the spectral intensities were estimated at 10% based on data reproducibility and observations from earlier STXM-XAS studies [47,54]. For all the spectra, uncertainty in the transition energies was estimated at ±0.2 eV for back-to-back measurements made during the same experimental campaign at the light sources. Due to the close proximity to each other and to the rising edge, some functions used to model higher energy features were affected by subtle changes in the curve-fitting model and an error of ±0.5 eV was assigned. The area under the preedge peaks (defined as the intensity) was calculated with the formula ph $\times$ fwhm $\times {}^1/_4 \times \{[\pi/\ln(2)]^{1/2} + \pi\}$, where ph = peak height (normalized intensity), fwhm = full-width at half-maximum height (eV), and the value ${}^1/_4 \times \{[\pi/\ln(2)]^{1/2} + \pi\} \approx 1.318$ is a constant associated with the pseudo-Voigt function.

D. Al K-edge spectral simulations

X-ray absorption near-edge spectroscopy (XANES) spectra at the Al K edge were simulated using the so-called excited-electron core-hole (XCH) approach [55], which has been described in detail elsewhere [55–57]. Briefly, within the XCH approach, the lowest energy excited state of the system is modeled within an occupation-constrained DFT framework employing a periodic supercell formalism. This is done by describing the core-excited atom within the supercell through a core-hole pseudopotential and taking into account the screening due to the excited electron self-consistently. Higher-lying x-ray excited-state energies are then approximated through eigenvalue differences obtained from the Kohn-Sham (KS) spectrum of the lowest energy core-excited state. X-ray transition matrix elements are calculated using Fermi's golden rule and typically for light-element K edges, employing the dipole approximation. The numerical implementation of the XCH method utilized in this study is based on a development version of the QUANTUM ESPRESSO package [58] that provides a plane-wave pseudopotential DFT framework for electronic structure calculations. Ultrasoft pseudopotentials [59] with the following valence electronic configurations: Al: [Ne]$3s^2 3p^1$; Yb: [Xe] $6s^2 4f^{14}$, Lu: [Xe] $6s^2 5d^1 4f^{14}$, were used together with a plane-wave energy cutoff of 50 Ry. To describe 1s core-excited Al in XANES simulations, a core-hole pseudopotential with the electronic configuration $1s^1 2s^2 2p^6 3s^2 3p^2$ was generated. The DFT calculations employed the Perdew-Burke-Ernzerhof [60] generalized-gradient approximation to describe exchange-correlation effects. XCH simulations of $M Al_2$ dialuminides employed $2 \times 2 \times 2$ supercells of the $MgCu_2$-type structure consisting of 192 atoms. Owing to the large size of supercells, the Brillouin zone was sampled through a $2 \times 2 \times 2$ Γ-centered k-point grid during the Kohn-Sham self-consistent field calculation, but the band structure was interpolated over a uniform Γ-centered $3 \times 3 \times 3$ k-point grid using the Shirley interpolation scheme [61] in order to generate XANES spectra. The XCH spectra were shifted rigidly by 1560.65 eV and the intensities scaled uniformly by 1.2×10^6 to facilitate comparison with experiment. A $4 \times 4 \times 4$ grid was used to generate the densities of states. XCH final state electronic wave functions corresponding to core excitations into the virtual orbital manifold were approximated by unoccupied KS wave functions obtained from the self-consistent occupation-constrained DFT calculation including the core hole. Orbital isosurfaces were visualized using VESTA-3 [62]. Band structures result in a large number of transitions for each unique value of k in the Brillouin zone, and isosurface plots were generated by isolating contributions to the band structure from the Γ point (0,0,0).

III. RESULTS

Figure 1 shows background-subtracted and normalized Al K-edge XAS for selected dialuminides and for an Al metal reference. Under the experimental conditions, the energy

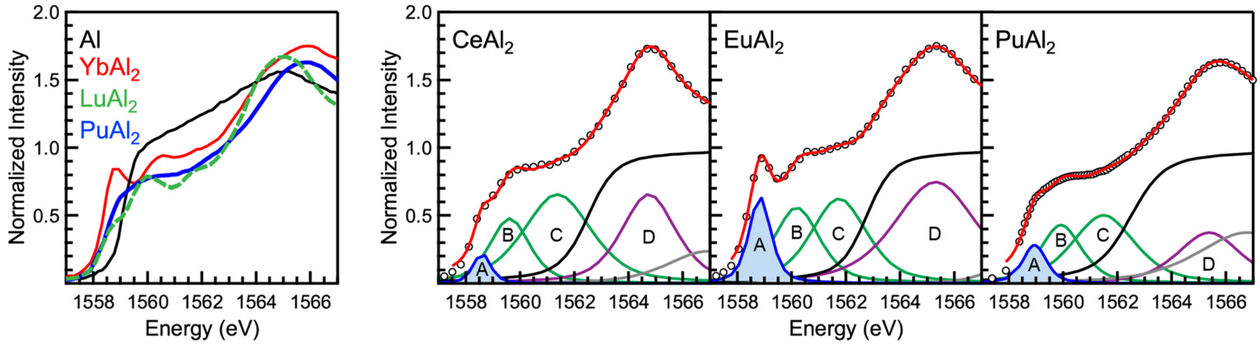

FIG. 1. (Left) Al K-edge XAS for $YbAl_2$, $LuAl_2$, $PuAl_2$, and Al metal (red, green, blue, and black). (Right) Curve fits (red) incorporating pseudo-Voigt functions (blue and pink) and step functions (black) for $CeAl_2$, $EuAl_2$, and $PuAl_2$. The $YbAl_2$ and $LuAl_2$ spectra are consistent with earlier Bremsstrahlung isochromat spectroscopy (BIS) results [63]. Additional spectra and fits for $SmAl_2$, $YbAl_2$, $LuAl_2$, and UAl_2 are provided in the Supplemental Material [64] and summarized in Table I.

resolution was estimated at 0.2 eV (see Methods). The Al K-edge spectra for each of the dialuminides and the Al reference foil are similar in that the onset of absorption intensity (first inflection point) occurs between 1558 and 1559 eV (Fig. 1). Within this low-energy regime, the edge onset for the dialuminides is an additional 0.4–0.8 eV lower in energy than observed for Al metal and intense, well-resolved features are observed for $EuAl_2$ and $YbAl_2$. To the best of our knowledge, the dialuminide edge onset energies are lower than have been observed for any other Al molecule or material. Moving to higher energies, one broad resonance is observed for all the dialuminides with energies that span a wide 1.5-eV energy range. For example, peak maxima occur near the bottom of the energy range at 1564.8 and 1564.6 for $CeAl_2$ and $SmAl_2$, respectively, while the peak maxima for $YbAl_2$ and $PuAl_2$ are found at higher energies of 1565.9 and 1565.8 eV, respectively. To quantify these effects, peaks in the experimental spectra were modeled using pseudo-Voigt functions and a step function with a 1:1 ratio of arctangent and error function contributions (Fig. 1 and Table I). Although mixing between the Al $3p$ and Ln or An f and d orbitals results in a large number of individual transitions, the first and second derivatives of the data suggest that four pseudo-Voigt functions provides the best fit to the edge region with the fewest parameters (or number of peaks).

TABLE I. Energies and intensities of pseudo-Voigt functions used in the spectral deconvolutions. Under the experimental conditions, the energy resolution was estimated at 0.2 eV (see Methods).

	Energies (eV); Intensities (area)			
	A	B	C	D[a]
$CeAl_2$	1558.6; 0.2	1559.6; 1.1	1561.4; 2.5	1564.8
$SmAl_2$	1558.5; 0.2	1559.5; 1.1	1561.2; 2.2	1564.6
$EuAl_2$	1558.8; 0.8	1560.2; 1.5	1561.7; 2.0	1565.3
$YbAl_2$	1558.8; 0.6	1560.1; 1.5	1561.9; 2.4	1565.9
$LuAl_2$	1558.7; 0.2	1559.9; 1.2	1561.8; 1.9	1565.0
UAl_2	1558.7; 0.5	1559.7; 1.0	1561.6; 1.9	1565.4
$PuAl_2$	1559.0; 0.4	1559.9; 1.0	1561.5; 1.8	1565.8

[a]Because the position and intensity of this feature varied with different curve-fitting models, energy values were determined from a plot of the 2nd derivative of the experimental spectrum.

The Al K-edge XAS were calculated using XCH-DFT to guide spectral interpretations. The XCH-DFT approach is advantageous because it provides accurate calculated spectra for large systems that can be compared directly to experimental data (Fig. 2). As discussed below, XCH-DFT calculations provide insights into the excited-state electronic structures of extended solids that are difficult to obtain using more computationally demanding methodologies on small-scale systems; additional calculations that can account for spin-orbit coupling and multiple-electron ground-state configurations are the subject of ongoing research. $YbAl_2$ and $LuAl_2$ were selected because both are reasonably well described by closed-shell $4f^{14}$ electronic configurations, and complications due to strong electron-electron correlations were minimized by freezing the $4f$ occupancy. The calculated and experimental spectra show excellent agreement with respect to both the relative energies and intensities of primary Al K-edge features. For example, the experimental results showed a threefold decrease in intensity for the low-energy A feature in the Al K-edge spectrum of $YbAl_2$ on moving to $LuAl_2$, from 0.6(1) to 0.2(1), while the maximum intensity of the XCH-DFT simulated spectrum at 1559.0 eV also decreased by a factor of 3, from 4.9×10^{-6} to 1.7×10^{-6}. Additionally, the postedge D feature was higher in energy for $YbAl_2$ (XAS: 1565.9 eV, XCH-DFT: 1566.4 eV) relative to $LuAl_2$ (XAS: 1565.0 eV; XCH-DFT: 1565.0 eV).

A unique advantage of the XCH-DFT approach for this work is that isosurface plots can be generated to visualize the electronic final states associated with individual Al K-edge transitions. Each isosurface represents an individual Kohn-Sham wave function selected from a continuum and is a qualitative reflection of the orbital character of the states. Figure 2 shows two isosurfaces associated with transitions near the low-energy A feature (1558.7 eV) and the high-energy D feature (1565.1 eV) for $LuAl_2$. The orbital character of individual atoms varies across each isosurface because the core-hole potential breaks the translational symmetry of the lattice. However, the two images depict (A) extended isosurface structures that are characteristic of Al $3p$ and Lu $5d$ bonding states at low energy and (D) localized isosurface structures that are characteristic of Al $3p$ and Lu $5d$ antibonding states at high energy. Taken together, the calculations support an intuitive band structure model where low-energy unoccupied states have bonding character and high-energy states have antibonding

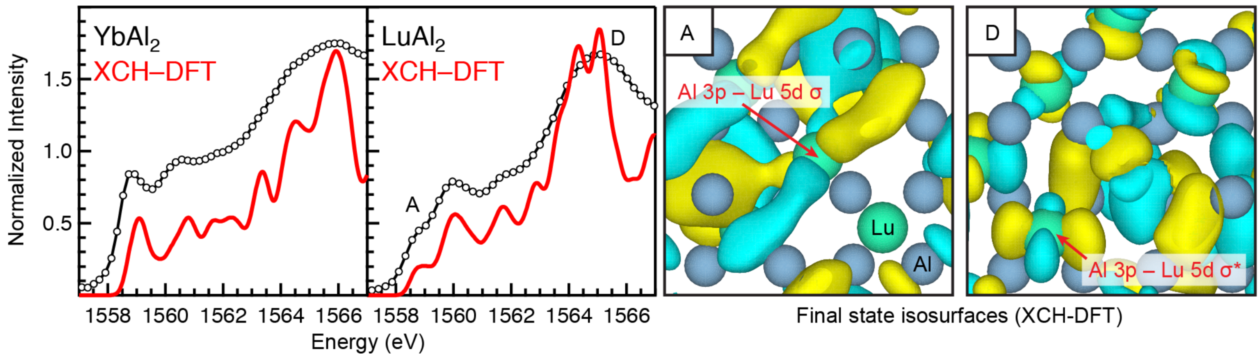

FIG. 2. (Left) Experimental and XCH-DFT simulated Al *K*-edge spectra for $YbAl_2$ and $LuAl_2$. Right, two orbital isosurfaces for $LuAl_2$ (A and D) that represent transitions near the features labeled "A" and "D" in the computed spectrum for $LuAl_2$. Arrows point to the most clearly visible Lu 5*d* orbitals in the orientations provided. The isosurfaces depict $\mathrm{sgn}(\psi)|\psi|^2$ for the real-valued orbitals at $k = 0$ and are plotted for 10% of the maximum absolute value, such that the blue and yellow colors depict changes in the sign of the wave function. Refer to the Supplemental Material [64] for $YbAl_2$ isosurfaces.

character. Within the bounds of this model, the low-energy A features near 1558.7 eV are assigned to transitions involving directional, σ-type Al 3*p*- and *Ln* 5*d*-orbital bonding. At higher energy, the broad D features observed at 1565.1 eV for $LuAl_2$ and at 1565.8 eV for $YbAl_2$ involve states derived from Al 3*p*- and *Ln* 5*d*-orbital σ antibonding. Isosurfaces associated with the features near 1560 eV (B and C in Fig. 1) are comprised of a complex mixture of nonbonding or less-directional π-type interactions between 3*p* orbitals on adjacent Al atoms or with the 5*d* orbitals on the Yb and Lu atoms. Aspects of this simple electronic structure model for $YbAl_2$ and $LuAl_2$ can be extrapolated to assign analogous features for $CeAl_2$, $SmAl_2$, $EuAl_2$, UAl_2, and $PuAl_2$.

The XCH-DFT calculations also determine the theoretical density of states (DOS) in the presence of a core hole. Figure 3 shows that the occupied 4*f* states are just below E_F for $YbAl_2$, and 6 eV below E_F for $LuAl_2$. These excited-state DOS results are in agreement with earlier optical conductivity measurements and ground-state theoretical studies on $YbAl_2$ and $LuAl_2$ [20]. For example, the Al 3*p* partial DOS for $YbAl_2$ indicates that the majority of the density up to 1 eV above E_F is associated with both Al 3*p* and Yb 5*d* states. A significant amount of Al 3*p* and Yb 5*d* density is also observed 7.5 eV above E_F. Like $YbAl_2$, the partial density of states (PDOS) for $LuAl_2$ also exhibits considerable density in a high-energy region 7 eV above E_F. However, considerably less Al 3*p* density is observed 1 eV above E_F for $LuAl_2$ relative to $YbAl_2$.

IV. DISCUSSION

Taken together, the experimental results, simulated spectra, orbital isosurfaces, and excited-state DOS all support a consistent picture of electronic structure in $Ln\mathrm{Al}_2$ and $An\mathrm{Al}_2$ compounds. As described above, the Al *K*-edge XAS and XCH-DFT show that intensities associated with low-energy transitions change significantly (A in Fig. 1), such that bonding interactions involving the Al 3*p* and *Ln* 5*d* or *An* 6*d* orbitals are greatest for $YbAl_2$ and $EuAl_2$, smallest for $CeAl_2$, $SmAl_2$, and $LuAl_2$, and intermediate for UAl_2 and $PuAl_2$. These changes also correlate with the destabilization of the Al 3*p* and *Ln* 5*d* or *An* 6*d* antibonding states, estimated from the position of the high-energy σ^* resonances (D in Fig. 1), which are roughly 0.5–1.0 eV higher in energy for $EuAl_2$, $YbAl_2$, UAl_2, and $PuAl_2$ relative to the other dialuminides (Table I). The experimental and XCH-DFT calculated Al *K*-edge transition intensities and energies also agree with the increase in density of Al 3*p* and Yb 5*d* states 1 eV above E_F for $YbAl_2$, and with the position of a maximum in the Al 3*p* and Yb 5*d* DOS at 7.5 eV for $YbAl_2$ compared with 7.0 eV for $LuAl_2$ (Fig. 3).

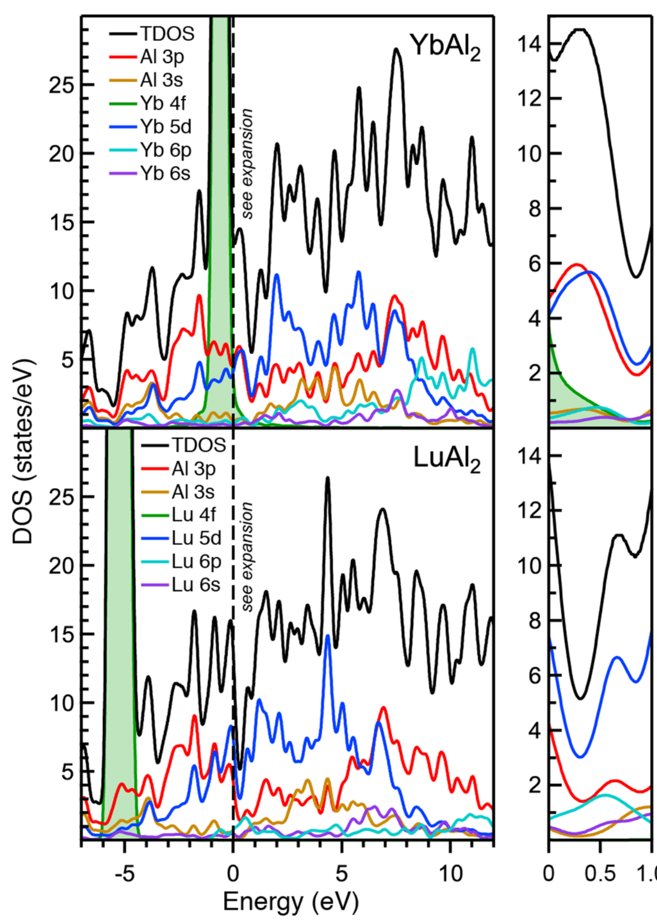

FIG. 3. The calculated DOS for $YbAl_2$ and $LuAl_2$. Expansions of the 1-eV region above E_F (right) highlight the increase in Al 3*p* and *Ln* 5*d* character for $YbAl_2$ relative to $LuAl_2$.

The relationship between the Al K-edge XAS results and ground-state electronic structure can be understood using a multielectron configuration interaction (CI) model which describes interactions between the Al $3p$, Ln $5d$, or An $6d$, and Ln $4f$ or An $5f$ orbitals in the ground state using the following expression:

$$\psi^* = N[a|f^n d^0 p^1\rangle + b|f^{n+1} d^0 p^0\rangle + c|f^n d^1 p^0\rangle + d|f^{n-1} d^1 p^1\rangle] \quad (1)$$

where N is the normalization constant and a, b, c, and d are mixing coefficients. The first configuration reflects no electron delocalization, such that n gives the f-orbital occupancy for a Ln^{3+} or An^{4+} ion (e.g., f^{13} for Yb^{3+} and f^4 for Pu^{4+}). The second and third configurations reflect hybridization with the Al $3p$ states resulting in charge transfer to either the f or d orbitals. The fourth configuration accounts for f-electron delocalization through mixing with the d states. If the electrons are predominantly localized, then the $f^n d^0 p^1$ configuration will have the largest contribution to the ground state [large a in Eq. (1)], and the preedge region in the Al K-edge XAS will resemble Al metal. More divalent character in the ground state [large b in Eq. (1)] and enhanced mixing with the Al $3p$ and Ln $5d$ [large c in Eq. (1)] results in charge transfer from the Al $3p$ states. Concomitantly, the probability of Al $1s \rightarrow 3p$ transitions for $EuAl_2$ and $YbAl_2$ increases and new Al K-edge features are observed.

The relationship between the CI model and the Al K-edge XAS and theory results can be understood further by considering earlier studies of the dialuminides. For example, calculations using the LDSA+U approach showed that while most LnAl$_2$ have FM ground states, $CeAl_2$ and $EuAl_2$ have AFM ground states and $YbAl_2$ is nonmagnetic [24]. Accordingly, $SmAl_2$ and $LuAl_2$ (both FMs) had weak low-energy Al K-edge features, suggesting that the ground states are dominated by the configuration with localized $4f$ electrons [large a in Eq. (1)]. In contrast, the Al K-edge XAS of $EuAl_2$ and $YbAl_2$ exhibited intense features at low energy. These features were indicative of Ln $5d$ and Al $3p$ mixing resulting from increased divalent character [large b and c in Eq. (1)] and reflected the lack of a magnetic moment for $YbAl_2$ and the AFM ground state for $EuAl_2$. $CeAl_2$ is unique in that an AFM ground state was calculated [24]; however, little evidence of Ce $5d$ and Al $3p$ mixing was obtained by Al K-edge XAS. We hypothesize that because the $4f^n$ states are higher in energy near the beginning of the lanthanide series, hybridization with the high-energy $5d$ states occurs in $CeAl_2$ without involving the Al $3p$ states [large d in Eq. (1)]. This alternate mechanism for electron delocalization explains how both $CeAl_2$ and $EuAl_2$ can have AFM ground states while only $EuAl_2$ exhibits the enhancement in Al $3p$ and Ln $5d$ hybridization probed by Al K-edge XAS. In different terminology, $EuAl_2$ and $YbAl_2$ engage in Al $3p$ mixing with the $4f^{n+1}$ states, while $CeAl_2$ mixes in the $4f^{n-1}$ state by hybridizing with the $5d$ orbitals.

The periodic changes in Al $3p$ hybridization with the $5d$ or $6d$ conduction bands described above can also be rationalized by developing a theoretical framework based on first-order perturbation theory (Fig. 4). Orbital mixing (λ) for a hypothetical MAl$_2$ molecule ($M = Ln$ or An) is described by

$$\lambda = S/(E^0_{\mathrm{M}} - E^0_{\mathrm{Al}}), \quad (2)$$

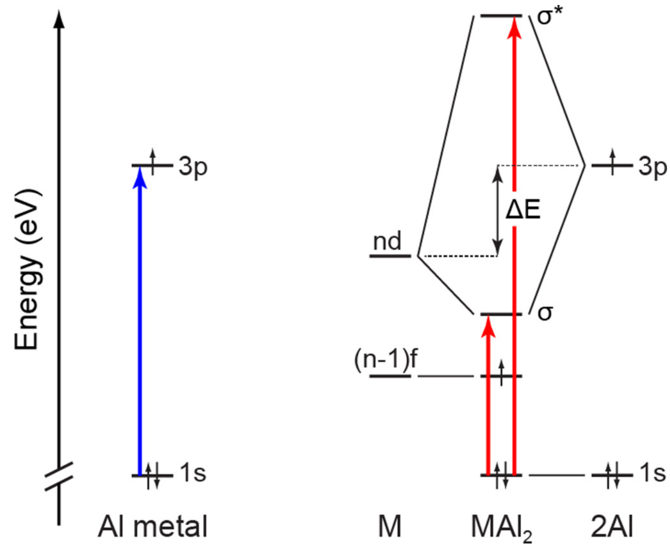

FIG. 4. Orbital correlation diagrams depicting the formation of new σ-bonding states in dialuminides upon mixing with the Al $3p$ and Ln or An d orbitals. Decreases in oxidation state (Ln^{3+} to Ln^{2+}) or increases in principle quantum number n ($5d$ to $6d$) result in higher d-orbital energies and enhanced mixing with the Al $3p$ orbitals for $EuAl_2$, $YbAl_2$, UAl_2, and $PuAl_2$ relative to $CeAl_2$, $SmAl_2$, and $LuAl_2$.

where S is the spatial overlap between atomic orbitals and $E^0_{\mathrm{M}} - E^0_{\mathrm{Al}}$ is their energy separation [65,66]. For $EuAl_2$ and $YbAl_2$, contributions from the divalent configuration (Ln^{2+}, $4f^{n+1}$) are increased relative to the normal trivalent configuration (Ln^{3+}, $4f^n$). In addition to increasing the ionic radius, this decrease in charge of the lanthanide atom destabilizes the $5d$ states. These two effects result in productive overlap (larger S) and a favorable energy match (small $E^0_{\mathrm{M}} - E^0_{\mathrm{Al}}$) with the high-energy Al $3p$ states (−6.0 eV). Because the Al 3p states are not completely filled in Al metal, this mixing results in formation of new Al $3p - Ln\,5d$ bonding states at lower energies, which are partially filled and sampled by Al K-edge XAS. For $CeAl_2$, $SmAl_2$, and $LuAl_2$, the increased contribution of the trivalent configuration stabilizes the $5d$ states and decreases ionic radii, resulting in both an energetic and spatial mismatch with the Al $3p$ states (large $E^0_{\mathrm{M}} - E^0_{\mathrm{Al}}$ and small S) and decreased M–Al mixing.

A similar model can be applied to UAl_2 and $PuAl_2$, where, to a first approximation, the ground-state electronic structure for U and Pu metals may be described by an interaction between two configurations, e.g., $5f^2$ and $5f^3$ for U^{4+} and U^{3+}, and $5f^5$ and $5f^6$ for Pu^{4+} and Pu^{3+} [67], respectively. Lanthanide and actinide $f \rightarrow d$ promotion energies and ionization energies suggest that the $5d^1$ and $6d^1$ states for Ln^{3+} and An^{4+} ions have similar energies [68–70]. Thus, the increase in Al $3p$ and An $6d$ mixing reflected by the Al K-edge XAS may result from an energetic match and from improved spatial overlap between the Al $3p$ and diffuse $6d$ atomic orbitals (small $E^0_{\mathrm{M}} - E^0_{\mathrm{Al}}$ and large S).

V. CONCLUSION

The results above show that Al K-edge XAS measured in transmission mode with STXM and combined with DFT calculations provides a probe of the dual nature of f-electron localization and itinerancy, using $Ln\mathrm{Al}_2$ and $An\mathrm{Al}_2$ as examples. The insights provided by Al K-edge XAS could not have been obtained easily from hard x-ray spectroscopies, magnetic measurements, or diffractive techniques. Our combined experimental and theoretical approach shows how f-orbital energies and occupancies can be tuned to change the energy of the *Ln* and *An* *d* orbitals, and indirectly impact the amount of σ and π mixing between the Al 3p orbitals. For CeAl_2, the Al 3p orbitals are largely unperturbed and 4f-electron delocalization occurs through direct mixing with the 5d states. An alternative mechanism is at work for EuAl_2 and YbAl_2, wherein mixing of the Al 3p orbitals into the conduction band facilitates 4f-electron delocalization and quenching of magnetic moments. Evidence for this latter mechanism is also observed for UAl_2 and PuAl_2, suggesting that Al 3p- and 6d-orbital mixing has an important role in mediating 5f electron behavior and magnetic properties. Furthermore, trends in the amount of Al 3p- and *Ln* or *An* *d*-orbital mixing are influenced by changes in spatial overlap. Given that overlap-driven orbital mixing is more strongly tied to stability [65], these findings are guiding our current efforts to enhance overlap with the diffuse 6d orbitals in new actinide materials with predictable phase stabilities and mechanical properties.

ACKNOWLEDGMENTS

This work was supported by the Director, Office of Science, Office of Basic Energy Sciences, Division of Chemical Sciences, Geosciences, and Biosciences Heavy Element Chemistry Program of the U.S. Department of Energy (DOE) at Lawrence Berkeley National Laboratory (LBNL) under Contract No. DE-AC02-05CH11231. A.B.A. also acknowledges support by a DOE Integrated University Program Fellowship at the University of California, Berkeley. Work at Los Alamos National Laboratory was performed under the auspices of the U.S. Department of Energy, Office of Basic Energy Sciences, Division of Materials Sciences and Engineering. The theory work of C.D.P. and D.G.P. was supported through a User Project at the Molecular Foundry of LBNL. Calculations were performed on the Cray XE6 Hopper computer at the National Energy Research Scientific Computing Center (NERSC-LBNL) and Molecular Foundry computing resources, Nano and Vulcan, managed by the High Performance Computing Services Group of LBNL. The lanthanide research described in this paper was performed at the Canadian Light Source, which is supported by the Canada Foundation for Innovation, Natural Sciences, and Engineering Research Council of Canada, the University of Saskatchewan, the Government of Saskatchewan, Western Economic Diversification Canada, the National Research Council Canada, and the Canadian Institutes of Health Research. Actinide research at beamline 11.0.2 at the ALS (T.T.) were supported by the Director, Office of Science, Office of Basic Energy Sciences, Division of Chemical Sciences, Geosciences, and Biosciences Condensed Phase and Interfacial Molecular Sciences Program of the U.S. DOE at LBNL under Contract No. DE-AC02-05CH11231.

[1] S. S. Hecker, Metall. Mater. Trans. A **35**, 2207 (2004).
[2] K. T. Moore and G. van der Laan, Rev. Mod. Phys. **81**, 235 (2009).
[3] J. L. Sarrao, L. A. Morales, J. D. Thompson, B. L. Scott, G. R. Stewart, F. Wastin, J. Rebizant, P. Boulet, E. Colineau, and G. H. Lander, Nature (London) **420**, 297 (2002).
[4] G. R. Stewart, Rev. Mod. Phys. **56**, 755 (1984).
[5] G. H. Lander, E. S. Fisher, and S. D. Bader, Adv. Phys. **43**, 1 (1994).
[6] S. L. Dudarev, D. N. Manh, and A. P. Sutton, Philos. Mag. B **75**, 613 (1997).
[7] D. J. Scalapino, Rev. Mod. Phys. **84**, 1383 (2012).
[8] E. D. Bauer and J. D. Thompson, Annu. Rev. Condens. Matter Phys. **6**, 137 (2015).
[9] H. G. Purwins and A. Leson, Adv. Phys. **39**, 309 (1990).
[10] K. Kang and M. Lee, Curr. Appl. Phys. **14**, 383 (2014).
[11] K. Buschow, Rep. Prog. Phys. **42**, 1373 (1979).
[12] F. Steglich, Physica C **460**, 7 (2007).
[13] B. A. Rao, P. Kistaiah, and K. S. Murthy, Mater. Lett. **9**, 410 (1990).
[14] B. A. Rao, P. Kistaiah, and K. S. Murthy, Phys. Status Solidi A **144**, K1 (1994).
[15] C. Dallera, E. Annese, J. P. Rueff, A. Palenzona, G. Vanko, L. Braicovich, A. Shukla, and M. Grioni, Phys. Rev. B **68**, 245114 (2003).
[16] K. A. Gschneidner, J. Less-Common Met. **17**, 13 (1969).
[17] E. E. Havinga, K. Buschow, and H. J. Van Daal, Solid State Commun. **13**, 621 (1973).
[18] F. Merlo, Thermochim. Acta **64**, 115 (1983).
[19] R. J. Lange, S. J. Lee, K. J. Kim, P. C. Canfield, and D. W. Lynch, Phys. Rev. B **63**, 035105 (2000).
[20] S. J. Lee, S. Y. Hong, I. R. Fisher, P. C. Canfield, B. N. Harmon, and D. W. Lynch, Phys. Rev. B **61**, 10076 (2000).
[21] J. Klaasse and J. Sterkenburg, Solid State Commun. **12**, 561 (1973).
[22] H. Wada and M. Shiga, Physica B **193**, 25 (1994).
[23] A. K. Pathak, D. Paudyal, K. A. Gschneidner, and V. K. Pecharsky, J. Appl. Phys. **115**, 17E109 (2014).
[24] D. Paudyal, V. K. Pecharsky, and K. A. Gschneidner, Jr., J. Appl. Phys. **115**, 17E127 (2014).
[25] D. Paudyal, A. K. Pathak, V. K. Pecharsky, and K. A. Gschneidner, J. Phys.: Condens. Matter **25**, 396002 (2013).
[26] T. Jarlborg, A. J. Freeman, and D. D. Koelling, J. Magn. Magn. Mater. **60**, 291 (1986).
[27] A. M. Boring, R. C. Albers, G. R. Stewart, and D. D. Koelling, Phys. Rev. B **31**, 3251 (1985).
[28] R. J. Trainor, M. B. Brodsky, and H. V. Culbert, Phys. Rev. Lett. **34**, 1019 (1975).
[29] A. T. Aldred, B. D. Dunlap, D. J. Lam, and I. Nowik, Phys. Rev. B **10**, 1011 (1974).
[30] G. R. Stewart and R. O. Elliott, Phys. Rev. B **31**, 4669 (1985).
[31] H. H. Hill, in *Plutonium 1970 and Other Actinides*, edited by W. N. Miner (AIME, New York, 1970).
[32] J. L. Smith and Z. Fisk, J. Appl. Phys. **53**, 7883 (1982).

[33] J. M. Wills and O. Erickson, Los Alamos Sci. **26**, 128 (2000).
[34] O. Keski-Rahkonen and M. O. Krause, At. Data Nucl. Data Tables **14**, 139 (1974).
[35] A. B. Altman, C. D. Pemmaraju, S. Alayoglu, J. Arnold, C. H. Booth, A. Braun, C. E. Bunker, A. Herve, S. G. Minasian, D. Prendergast, D. K. Shuh, and T. Tyliszczak, Inorg. Chem. **56**, 5710 (2017).
[36] A. Benuzzi-Mounaix, F. Dorchies, V. Recoules, F. Festa, O. Peyrusse, A. Levy, A. Ravasio, T. Hall, M. Koenig, N. Amadou, E. Brambrink, and S. Mazevet, Phys. Rev. Lett. **107**, 165006 (2011).
[37] P. Ildefonse, D. Cabaret, P. Sainctavit, G. Calas, A. M. Flank, and P. Lagarde, Phys. Chem. Miner. **25**, 112 (1998).
[38] T. H. Yoon, S. B. Johnson, K. Benzerara, C. S. Doyle, T. Tyliszczak, D. K. Shuh, and G. E. Brown, Langmuir **20**, 10361 (2004).
[39] J. A. van Bokhoven and C. Lamberti, Coord. Chem. Rev. **277**, 275 (2014).
[40] L. R. Aramburo, Y. Liu, T. Tyliszczak, F. M. F. de Groot, J. C. Andrews, and B. M. Weckhuysen, ChemPhysChem **14**, 496 (2013).
[41] H. E. van der Bij, D. Cicmil, J. Wang, F. Meirer, F. M. F. de Groot, and B. M. Weckhuysen, J. Am. Chem. Soc. **136**, 17774 (2014).
[42] A. B. Altman, C. D. Pemmaraju, C. Camp, J. Arnold, S. G. Minasian, D. Prendergast, D. K. Shuh, and T. Tyliszczak, J. Am. Chem. Soc. **137**, 10304 (2015).
[43] C. P. Balde, A. E. Mijovilovich, D. C. Koningsberger, A. M. J. van der Eerden, A. D. Smith, K. P. de Jong, and J. H. Bitter, J. Phys. Chem. C **111**, 11721 (2007).
[44] T. Sikora, G. Hug, M. Jaouen, and J. J. Rehr, Phys. Rev. B **62**, 1723 (2000).
[45] A. J. Arko, F. Y. Fradin, and M. B. Brodsky, Phys. Rev. B **8**, 4104 (1973).
[46] C. H. Booth, Y. Jiang, S. A. Medling, D. L. Wang, A. L. Costello, D. S. Schwartz, J. N. Mitchell, P. H. Tobash, E. D. Bauer, S. K. McCall, M. A. Wall, and P. G. Allen, J. Appl. Phys. **113**, 093502 (2013).
[47] S. G. Minasian, J. M. Keith, E. R. Batista, K. S. Boland, J. A. Bradley, S. R. Daly, D. Sokaras, S. A. Kozimor, W. W. Lukens, R. L. Martin, D. Nordlund, G. T. Seidler, D. K. Shuh, T. Tyliszczak, G. L. Wagner, T. C. Weng, and P. Yang, J. Am. Chem. Soc. **135**, 1864 (2013).
[48] K. V. Kaznatcheev, C. Karunakaran, U. D. Lanke, S. G. Urquhart, M. Obst, and A. P. Hitchcock, Nucl. Instrum. Methods Phys. Res. **582**, 96 (2007).
[49] H. Bluhm, K. Andersson, T. Araki, K. Benzerara, G. E. Brown, J. J. Dynes, S. Ghosal, M. K. Gilles, H. C. Hansen, J. C. Hemminger, A. P. Hitchcock, G. Ketteler, A. L. D. Kilcoyne, E. Kneedler, J. R. Lawrence, G. G. Leppard, J. Majzlan, B. S. Mun, S. C. B. Myneni, A. Nilsson, H. Ogasawara, D. F. Ogletree, K. Pecher, M. Salmeron, D. K. Shuh, B. Tonner, T. Tyliszczak, T. Warwick, and T. H. Yoon, J. Electron. Spectrosc. Relat. Phenom. **150**, 86 (2006).
[50] A. L. D. Kilcoyne, T. Tyliszczak, W. F. Steele, S. Fakra, P. Hitchcock, K. Franck, E. Anderson, B. Harteneck, E. G. Rightor, G. E. Mitchell, A. P. Hitchcock, L. Yang, T. Warwick, and H. Ade, J. Synchrotron Radiat. **10**, 125 (2003).
[51] H. J. Nilsson, T. Tyliszczak, R. E. Wilson, L. Werme, and D. K. Shuh, Anal. Bioanal. Chem. **383**, 41 (2005).
[52] T. C. Weng, G. S. Waldo, and J. E. Penner-Hahn, J. Synchrotron Radiat. **12**, 506 (2005).
[53] G. N. George, EDG_FIT, Stanford, CA.
[54] S. G. Minasian, J. M. Keith, E. R. Batista, K. S. Boland, S. A. Kozimor, R. L. Martin, D. K. Shuh, T. Tyliszczak, and L. J. Vernon, J. Am. Chem. Soc. **135**, 14731 (2013).
[55] D. Prendergast and G. Galli, Phys. Rev. Lett. **96**, 215502 (2006).
[56] A. H. England, A. M. Duffin, C. P. Schwartz, J. S. Uejio, D. Prendergast, and R. J. Saykally, Chem. Phys. Lett. **514**, 187 (2011).
[57] C. D. Pemmaraju, R. Copping, S. Wang, M. Janousch, S. J. Teat, T. Tyliszcak, A. Canning, D. K. Shuh, and D. Prendergast, Inorg. Chem. **53**, 11415 (2014).
[58] P. Giannozzi, S. Baroni, N. Bonini, M. Calandra, R. Car, C. Cavazzoni, D. Ceresoli, G. L. Chiarotti, M. Cococcioni, I. Dabo, A. Dal Corso, S. de Gironcoli, S. Fabris, G. Fratesi, R. Gebauer, U. Gerstmann, C. Gougoussis, A. Kokalj, M. Lazzeri, L. Martin-Samos, N. Marzari, F. Mauri, R. Mazzarello, S. Paolini, A. Pasquarello, L. Paulatto, C. Sbraccia, S. Scandolo, G. Sclauzero, A. P. Seitsonen, A. Smogunov, P. Umari, and R. M. Wentzcovitch, J. Phys.: Condens. Matter **21**, 395502 (2009).
[59] D. Vanderbilt, Phys. Rev. B **41**, 7892 (1990).
[60] J. P. Perdew, K. Burke, and M. Ernzerhof, Phys. Rev. Lett. **77**, 3865 (1996).
[61] D. Prendergast and S. G. Louie, Phys. Rev. B **80**, 235126 (2009).
[62] K. Momma and F. Izumi, J. Appl. Crystallogr. **44**, 1272 (2011).
[63] S. J. Oh, J. W. Allen, M. S. Torikachvili, and M. B. Maple, J. Magn. Magn. Mater. **52**, 183 (1985).
[64] See Supplemental Material at http://link.aps.org/supplemental/10.1103/PhysRevB.97.045110 for additional spectra and STXM images.
[65] S. G. Minasian, J. M. Kieth, E. R. Batista, K. S. Boland, C. N. Christensen, D. L. Clark, S. D. Conradson, S. A. Kozimor, R. L. Martin, D. E. Schwarz, D. K. Shuh, G. L. Wagner, M. P. Wilkerson, L. E. Wolfsberg, and P. Yang, J. Am. Chem. Soc. **134**, 5586 (2012).
[66] I. D. Prodan, G. E. Scuseria, and R. L. Martin, Phys. Rev. B **76**, 033101 (2007).
[67] C. H. Booth, Y. Jiang, D. L. Wang, J. N. Mitchell, P. H. Tobash, E. D. Bauer, M. A. Wall, P. G. Allen, D. Sokaras, D. Nordlund, T. C. Weng, M. A. Torrez, and J. L. Sarrao, PNAS **109**, 10205 (2012).
[68] L. Brewer, J. Opt. Soc. Am. **61**, 1666 (1971).
[69] W. C. Martin, R. Zalubas, and L. Hagan, *Atomic Energy Levels—The Rare Earth Elements*, NSRDS-NBS 60 (National Bureau of Standards, U.S. Department of Commerce, Washington, DC, 1978).
[70] X. Y. Cao and M. Dolg, J. Mol. Struct. **673**, 203 (2004).